Experimental Investigation of High-Mach-Number 3D Hydrodynamic Jets at the National Ignition Facility

B. E. Blue,[1] S. V. Weber,[1] S. G. Glendinning,[1] N. E. Lanier,[2] D. T. Woods,[1] M. J. Bono,[1] S. N. Dixit,[1] C. A. Haynam,[1] J. P. Holder,[1] D. H. Kalantar,[1] B. J. MacGowan,[1] A. J. Nikitin,[1] V. V. Rekow,[1] B. M. Van Wonterghem,[1] E. I. Moses,[1] P. E. Stry,[1] B. H. Wilde,[2] W. W. Hsing,[1] and H. F. Robey[1]

[1]*Lawrence Livermore National Laboratory, Livermore, California 94550, USA*
[2]*Los Alamos National Laboratory, Los Alamos, New Mexico 87545, USA*

(Received 11 October 2004; published 11 March 2005)

The first hydrodynamic experiments were performed on the National Ignition Facility. A supersonic jet was formed via the interaction of a laser driven shock (~ 40 Mbar) with 2D and 3D density perturbations. The temporal evolution of the jet's spatial scales and ejected mass were measured with point-projection x-ray radiography. Measurements of the large-scale features and mass are in good agreement with 2D and 3D numerical simulations. These experiments provide quantitative data on the evolution of 3D supersonic jets and provide insight into their 3D behavior.

DOI: 10.1103/PhysRevLett.94.095005 PACS numbers: 52.35.Tc, 52.50.Jm, 52.57.–z

The interaction of a shock wave with a density perturbation is a problem of basic scientific interest [1] with specific application to astrophysics [2] and inertial confinement fusion (ICF) [3]. For instance, high-Mach number hydrodynamic jets, which can result from a shock-perturbation interaction, are ubiquitous features of supernovae in astrophysics [4–7] and may result from the presence of capsule joints or cryogenic fill tubes in ICF [8]. Although the spatial scales of these systems vary over 16 orders of magnitude from supernovae jets ($\sim 10^{10}$ m) to micron scale jets inside ICF capsules, they are unified by the physics of a high-Mach number shock interacting with a perturbation at a two fluid interface. In both systems the shock-perturbation interaction results in a jet of plasma being ejected ahead of the shocked material interface. In the case of supernovae, a jet provides a possible mechanism for explaining the observation of the early appearance of core high Z elements (nickel, iron, etc) [9] in the outer helium and hydrogen envelope. In the case of ICF capsules, fabrication joints or fill tubes can mix cooler shell material into the fuel before optimal compression, possibly affecting ignition [8]. Previous work has studied the spatial evolution of 2D jets [6]. This Letter describes quantitative measurement of the evolution of 3D supersonic jets and provides insight into their 3D behavior. To validate the simulations of these phenomena, there are several parameters of critical importance. They are the spatial dimensions, the characteristic velocities, the total mass of material, and the spatial mass distribution of the jet material.

An experiment was conducted to investigate jet formation in 2D and 3D shocked systems using the first quad (four beams) of the National Ignition Facility (NIF) [10,11] located at Lawrence Livermore National Laboratory. A 1.5 ns, 6 kJ (2×3 kJ beams), 3ω (351 nm wavelength), 1000 μm diameter laser pulse (4×10^{14} W/cm^2) was used to drive a 40 Mbar shock wave into aluminum targets backed by 100 mg/cc carbon aerogel foam. The experimental package consisted of a 101 ± 2 μm thickness aluminum disk placed in direct contact with a second aluminum disk of 149 ± 2 μm thickness that contained a central, 162 ± 2 μm diameter hole. The hole was drilled at either 0° for the case of a two-dimensional cylindrically symmetric target [Fig. 1(a)] or 45° for the case of a fully three-dimensional target [Fig. 1(b)]. The two 800 μm diameter aluminum disks were inserted into a 2000 μm diameter, 250 μm thick gold washer that delayed the propagation of shocks around the exterior of the target package. The front surface of the target was coated with a 57 ± 2 μm thick polystyrene ablator. The carbon aerogel was encased in a polystyrene shock tube with a wall thickness of 40 μm.

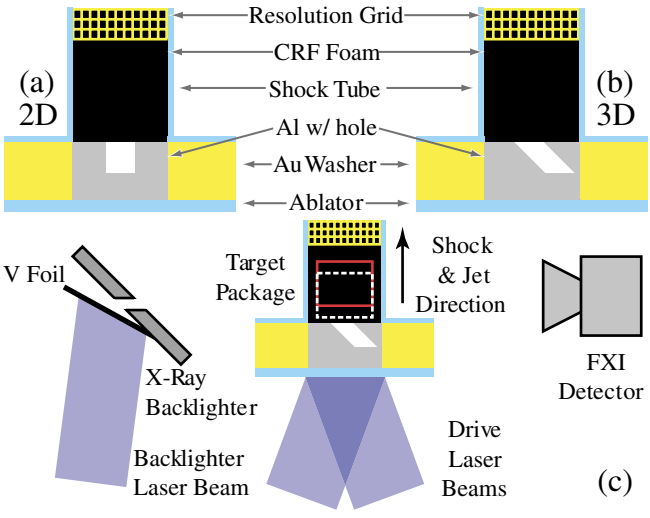

FIG. 1 (color). Schematic of a 2D target (a), a 3D target (b), and the radiographic configuration used on NIF (c) (not to scale).

The hydrodynamic evolution of the target package was diagnosed with pinhole-apertured point-projection radiography [12] [Fig. 1(c)]. An additional 1.5 ns, 2.5 kJ, 3ω, 500 μm diameter laser pulse (6.7×10^{14} W/cm^2) illuminated the rear side of a 5 μm thick vanadium foil in order to create a 5.2 keV x-ray source. This backlighter laser pulse was delayed either 16 or 22 ns after the drive-laser pulse so that the evolution of the target package could be imaged at two points in time. The 500 μm diameter x-ray source was apertured by a 20 μm diameter pinhole in a 50 μm thick, tantalum substrate to create a point source of x rays. The point source was imaged through the experimental target onto a gated microchannel plate flexible x-ray imager (FXI) [13] with a magnification of 20. A 230 ps gate window was timed to capture a snapshot of the jet's hydrodynamic evolution during the backlighter pulse with minimal motion blurring ($\sim$7 μm) while rejecting drive-laser generated x rays which would increase the noise level of the image. The FXI was filtered with 18 μm of aluminum that transmitted the 5.2 keV vanadium x-ray line while attenuating lower energy x rays. An additional 125 μm of Kapton was used in the filter package to protect the FXI from debris.

Laser ablation of the plastic ablator covering the planar aluminum surface results in a high-pressure shock propagating in the Al. This shock heats the Al to the point where it becomes a plasma, and as the shock passes the hole in the Al, Al plasma fills the low-pressure hole. This Al plasma then expands into the foam in the form of a supersonic jet. Figure 2 shows the experimental radiographs of both the 2D and 3D targets at $t = 16$ and 22 ns. Each radiograph was acquired on a separate target and laser shot. In all of the radiographs, the gray scale used depicts the optically thick Al as a black or dark gray and the optically thin foam as a light gray color. The spatial scale of the resultant structure was calibrated to a reference grid on the target that consisted of 21 μm Au wires with a period of 63.5 μm. The contrast of the shock front exhibits some enhancement due to refraction [14]. All images show a pedestal of Al flowing down the shock tube, a compressed region of foam preceding the Al pedestal, a jet of Al propagating into the uncompressed foam, and the jet's associated bow shock. The frame of each image was shifted so that it tracked the pedestal and jet motion down the shock tube. Figure 1(c) shows the approximate frame location of the 16 ns data as a dashed white rectangle and that of the 22 ns data as a solid red one. The spatial scale on all images is 730 μm wide by 560 μm tall.

In addition to the spatial scales and velocities, it is important to quantify the mass of ejected material and its areal distribution. The mass calculation used conservation of mass to account for the mass of shocked foam preceding the Al pedestal. The difference in transmitted intensity in a region ahead of the shock will be related to the total mass of Al and of the foam pushed up by the pedestal. Regardless of symmetry, the total Al mass is given by

$$m_{\mathrm{Al}} = \frac{-1}{\mu_{\mathrm{Al}}}\left[\int_S \ln\left(\frac{I}{I_0}\right) dS + \mu_f m_f\right]. \quad (1)$$

Here m_{Al}, m_f, μ_{Al}, μ_f, S, I, and I_0 are , respectively, the measured Al mass, the mass of the foam displaced by the pedestal, the Al mass absorption coefficient, the foam mass absorption coefficient, the surface over which the mass is calculated, the transmitted intensity, and the transmitted intensity through the uncompressed foam. This method results in a measurement of the total Al mass since it

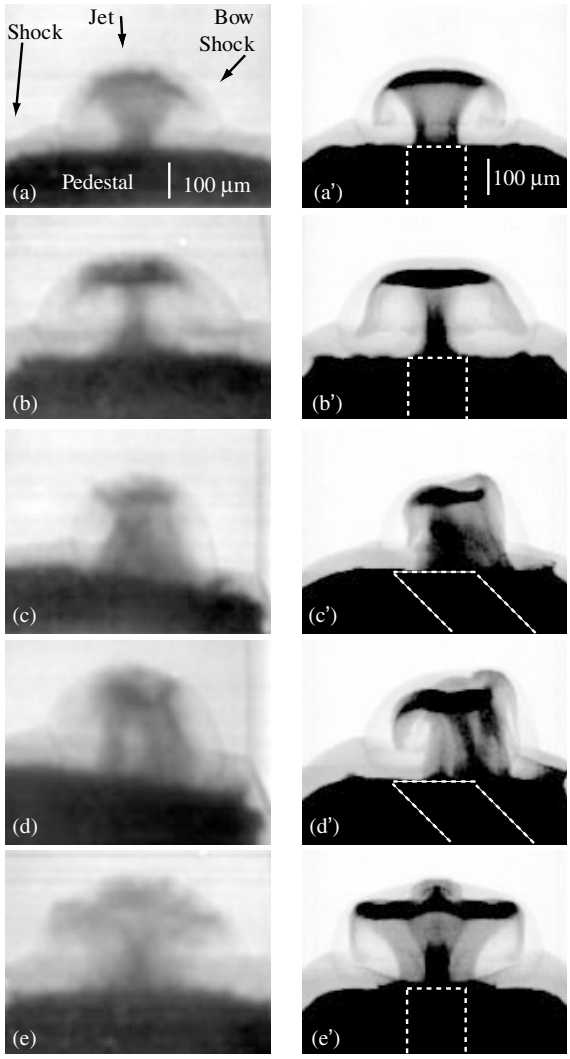

FIG. 2. Experimental and simulated radiographs of 2D and 3D jet targets. Experimental data are shown on the left (a)–(e) and the corresponding simulated radiographs are shown on the right (a′)–(e′). The 2D jet is shown at $t = 16$ (a),(a′) and 22 ns (b),(b′). The asymmetric view of the 3D jet is shown at $t = 16$ ns (c),(c′) and $t = 22$ ns (d),(d′). The symmetric view of the 3D jet at $t = 22$ ns is shown in (e),(e′). The dashed white lines in the simulated radiographs are the outlines of the preshocked holes offset upwards to the pedestal-foam interface.

removes the contribution of the compressed foam. The areal mass distribution of Al was estimated by assuming that the attenuation of x-ray intensity at each pixel was solely due to Al. A suitable region of interest (ROI) was used around the jet to minimize the contribution of compressed foam. The formula used to calculate the Al areal mass distribution is

$$M_{\mathrm{Al}}(r, z) = \frac{-A}{\mu_{\mathrm{Al}}} \ln\left(\frac{I(r, z)}{I_0}\right). \quad (2)$$

Here r and z are the spatial coordinates of a pixel with area A in which the mass is calculated. This measurement includes a contribution from compressed foam. Because of the lower density and opacity of the compressed foam and the use of a suitable ROI to minimize its contribution, the inclusion of the foam did not significantly affect the measurement of the Al mass distribution.

Figures 2(a) and 2(b) show the evolution of a 2D jet at 16 and 22 ns, respectively, while Figs. 2(c)–2(e) show the evolution of 3D jets at 16 and 22 ns. In order to diagnose the 3D jet, radiographs from two orthogonal views were obtained. Figures 2(c) and 2(d) show the 16 and 22 ns asymmetric views, respectively, in which the tilt of the hole is in the plane of the image. Figure 2(e) shows the orthogonal, symmetric view at 22 ns in which the axis of the hole points at a 45° angle out of the page. Figure 2(e) is complementary to Fig. 2(d) in that both imaged equivalent jets (identical targets on different shots) from two orthogonal views so that the complicated 3D fluid flow could be understood.

The experiment was modeled with the 3D, arbitrary Lagrange Euler (ALE) radiation hydrocode HYDRA [15]. The simulation consisted of a $410 \times 293 \times 147$ mesh covering a simulation region of 2.0 mm $\times$ 2.0 mm $\times$ 2.5 mm with grid sizes as small as 4 μm. The simulation is ALE, but relaxation kept the mesh in the jet approximately Cartesian. The measured 3D laser spatial intensity profile was included to more accurately model the experiment. Radiation transport was modeled in the gray diffusion approximation and the equations of state were generated off-line and input in tabular form. Figures 2(a′)–2(e′) show simulated radiographs of both the 2D and 3D simulation results at 16 and 22 ns. The spatial scales are equivalent to the experimental data shown in Figs. 2(a)–2(e). The dashed white lines are the outlines of the preshocked holes offset upwards to the pedestal-foam interface. Figure 2(a′) shows a 2D jet at 16 ns and Fig. 2(b′) shows one at 22 ns. Figures 2(c′) and 2(d′) show the 16 and 22 ns asymmetric views of the 3D target. Figure 2(e′) shows the orthogonal symmetric view of the 3D jet at 22 ns.

Table I summarizes the key quantitative measurements from the experiment and the simulations. The jet distance is the distance the tip of the jet has propagated ahead of the pedestal. The jet velocity was measured by a linear extrapolation of the jet distances measured from the original Al-foam interface at the two different times. The mass is the total mass of Al ahead of the pedestal. The error bars in the positional measurements are due to the pinhole limited 20 μm spatial resolution. The error in the mass is due to the FXI induced noise and background levels of the data.

Significant differences exist between the 2D and 3D jets. First, the 2D jet is aligned along the axis of the hole in the Al disk while, counterintuitively, the mass of the 3D jet is not ejected along the axis of the hole. In the regime of strong shocks, the mass flow is controlled by the shock trajectory and thus the mass is ejected approximately normal to the shock. A second difference is that the 3D jet has a considerably more complicated structure and is more diffuse than the 2D jets suggesting that the 3D structure is more unstable than the 2D. The 2D jet has a clearly defined head and stem. The fan-shaped stem of the 2D jet at 16 ns [Fig. 2(a)] expands from 92 ± 20 μm at the jet-pedestal interface to 234 ± 20 μm at the head of the jet. The width of the jet at its base is less than the original hole diameter of 161 μm because the hole is collapsing on axis. This collapse increases the pressure in the hole, thus imparting energy to the jet to launch it ahead of the nominal interface. At 22 ns, the 2D jet's stem [Fig. 2(b)] has formed a well-defined cylindrical shape. The head of the 2D jet is wider and symmetric about the axis. The 3D jet does not possess a well-defined stem and head. As opposed to the 2D case, the stem of the 3D jet is as wide as the head in the asymmetric view [Figs. 2(c) and 2(d)], while it is smaller than the head in the symmetric view [Fig. 2(e)]. The width of the 3D jet's head, as viewed in the symmetric view, is $\sim$50% greater than that of the 2D jet.

Figure 3 summarizes key results of the jet's mass evolution. Figure 3(a) shows how much total mass was ejected by the 2D (blue circles) and 3D (red squares) perturbations. The solid lines are from the simulations. The 3D jets ejected more mass than the 2D jets by a factor of $\sim\sqrt{2}$, the ratio of the hole volumes. Simulations in which a 3D target had a hole volume equal to a 2D target confirmed this since both ejected masses were observed to be the same. Figure 3(b) shows the areal center of mass within the jet at 22 ns as a function of distance ahead of the pedestal from the experimental data. The yellow and green bars are the

TABLE I. Summary of three key metrics of the jet evolution from both the experiment and the simulations: the distance the jet has advanced ahead of the pedestal, the velocity of the jet, and the mass of Al in the jet.

	2D Target		3D Target	
Measurement	Exp.	Sim.	Exp.	Sim.
Distance @ 16 ns (μm)	216 ± 28	195	255 ± 28	230
Distance @ 22 ns (μm)	250 ± 28	232	300 ± 28	272
Jet velocity (km/s)	29.5 ± 3.3	33.9	35.1 ± 3.3	37.0
Mass @ 16 ns (μg)	2.9 ± 0.8	3.47	3.6 ± 0.8	4.77
Mass @ 22 ns (μg)	4.5 ± 0.8	3.98	6.1 ± 0.8	5.62

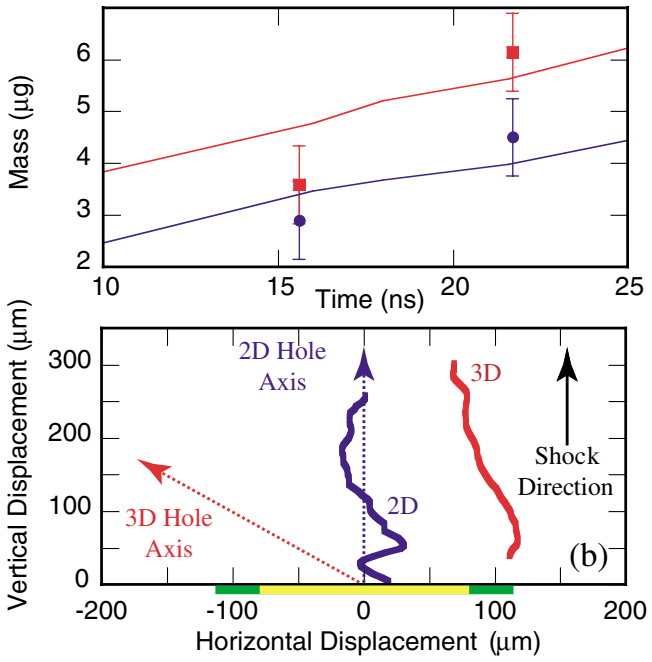

FIG. 3 (color). Key results of the jet's mass evolution from both the experiment and the simulations: the mass of Al in the jet (a) and the areal center of mass within the jet at 22 ns as a function of distance ahead of the pedestal from experimental data (b). The 2D experimental data are shown as blue circles and the 3D as red squares. The simulation results are shown as blue and red lines for the 2D and 3D jets, respectively, in (a). The yellow and green bars are the diameters of the 2D and 3D holes at the Al-foam interface, respectively.

locations and dimensions of the 2D and 3D holes at the Al pedestal-foam interface, respectively. The 2D jet data (blue) shows that the jet was distributed symmetrically around the hole axis (blue arrow) near the head (vertical displacement $\sim 250\ \mu$m), but it deviated in the lower part of the stem. This deviation is due to a tilt on the pedestal interface that led to an asymmetric shock (and therefore material) breakout at the Al-foam interface as seen in Fig. 2(b). The 3D jet's distribution of mass (red line) did not follow the axis of the hole (red arrow); rather it propagates essentially along the shock trajectory. As viewed from the major metrics of the jet evolution (velocity, distance, and mass), excellent agreement was found between simulations and experiment. However, differences in the small-scale flow patterns and the distribution of mass inside of the jets do exist. This is expected since the Reynolds numbers of the jets are very large ($\sim 10^7$, which is in the strongly turbulent regime), the effective numerical Reynolds numbers of the simulations are orders of magnitude lower (limited by computational power), and therefore the simulations do not accurately model the experiment. These differences are more pronounced in the 3D jets as opposed to the 2D jets. This is consistent with the observation that the 3D flow has a fully three-dimensional vorticity field, whereas in the 2D case, the vorticity is nonzero only in the azimuthal component. The 3D jets can transition to a turbulent state faster since the 2D jets need time for instabilities to break symmetry and seed the three-dimensional vorticity field.

These results aid our understanding of the complex hydrodynamics in supernovae and also of the physical processes relevant to ignition of NIF ICF capsules. In the case of astrophysics, two examples are jet-induced supernovae [7] and Rayleigh-Taylor mixing, in which each outwardly propagating spike effectively acts as an isolated jet [16]. Experimental data on 2D and 3D jets with relevant parameters to astrophysics [17] can be used to benchmark supernovae simulations. For the ICF application, these results are also of interest as they demonstrate clear differences in jet shape, velocity, and ejected mass distribution as a function of perturbation geometry. Such differences should be considered in the design of capsule fabrication features to minimize their impact on ignition on facilities such as NIF.

The authors wish to thank the staff at NIF for their assistance in performing this experiment. We also wish to thank H. Louis, D. O'Brien, and R. Wallace for their work in target fabrication. This work was performed under the auspices of the U.S. Department of Energy by Los Alamos National Laboratory under Contract No. W-7405-ENG-36 and by Lawrence Livermore National Laboratory under Contract No. W-7405-ENG-48.

[1] R. C. Davidson *et al.*, *Frontiers in High Energy Density Physics: The X-Games of Contemporary Science* (The National Academies Press, Washington, DC, 2003).
[2] H. F. Robey *et al.*, Phys. Rev. Lett. **89**, 085001 (2002).
[3] J. D. Lindl, Phys. Plasmas **2**, 3933 (1995).
[4] B. Reipurth and J. Bally, Annu. Rev. Astron. Astrophys. **39**, 403 (2001).
[5] V. Icke *et al.*, Nature (London) **355**, 524 (1992).
[6] J. M. Foster *et al.*, Phys. Plasmas **9**, 2251 (2002).
[7] A. M. Khokhlov *et al.*, Astrophys. J. Lett. **524**, L107 (1999).
[8] S. R. Goldman *et al.*, Phys. Plasmas **6**, 3327 (1999).
[9] L. Wang *et al.*, Astrophys. J. **579**, 671 (2002).
[10] J. A. Paisner *et al.*, Laser Focus World **30**, 75 (1994).
[11] The initial four beams of NIF beams were available for this experiment. When completed, NIF will use up to 192 beams for experiments.
[12] J. Workman *et al.*, Rev. Sci. Instrum. **75**, 3915 (2004).
[13] K. S. Budil *et al.*, Rev. Sci. Instrum. **67**, 485 (1996).
[14] D. Montgomery *et al.*, Rev. Sci. Instrum. **75**, 3986 (2004).
[15] M. M. Marinak *et al.*, Phys. Plasmas **3**, 2070 (1996).
[16] K. Kifonidis *et al.*, Astron. Astrophys. **408**, 621 (2003).
[17] D. Ryutov *et al.*, Astrophys. J. **518**, 821 (1999).